UC Berkeley
UC Berkeley Previously Published Works

Title
High-Performance Atomically-Thin Room-Temperature NO2 Sensor

Permalink
https://escholarship.org/uc/item/2cn021j3

Journal
Nano Letters, 20(8)

ISSN
1530-6984

Authors
Azizi, Amin
Dogan, Mehmet
Long, Hu
et al.

Publication Date
2020-08-12

DOI
10.1021/acs.nanolett.0c02221

Peer reviewed

eScholarship.org Powered by the California Digital Library
University of California

High-Performance Atomically-Thin Room-Temperature NO_2 Sensor

Amin Azizi[1,2], Mehmet Dogan[1,3], Hu Long[1,2,3], Jeffrey D. Cain[1,2,3], Kyunghoon Lee[1,2,3], Rahmatollah Eskandari[1], Alessandro Varieschi[1], Emily C. Glazer[1], Marvin L. Cohen[1,3], Alex Zettl*[,1,2,3]

1. *Department of Physics, University of California at Berkeley, Berkeley, CA, 94720, USA*
2. *Kavli Energy NanoScience Institute at the University of California, Berkeley, Berkeley, CA, 94720, USA*
3. *Materials Sciences Division, Lawrence Berkeley National Laboratory, Berkeley, CA, 94720, USA*

* Corresponding Author. E-mail: azettl@berkeley.edu , Phone: +1 (510) 642-4939 Fax: +1 (510) 642-2685

Abstract:

The development of room-temperature sensing devices for detecting small concentrations of molecular species is imperative for a wide range of low-power sensor applications. We demonstrate a room-temperature, highly sensitive, selective, and reversible chemical sensor based on a monolayer of the transition metal dichalcogenide $Re_{0.5}Nb_{0.5}S_2$. The sensing device exhibits thickness dependent carrier type, and upon exposure to NO_2 molecules, its electrical resistance considerably increases or decreases depending on the layer number. The sensor is selective to NO_2 with only minimal response to other gases such as NH_3, CH_2O, and CO_2. In the presence of humidity, not only are the sensing properties not deteriorated, but also the monolayer sensor shows complete reversibility with fast recovery at room temperature. We present a theoretical analysis of the sensing platform and identify the atomically-sensitive transduction mechanism.

Chemical sensing devices are crucial to monitoring environmental pollution, health conditions, and industrial processes. In particular, the detection of nitrogen dioxide (NO_2), a toxic gas emitted from power plants, vehicles, and industrial sources, is of significant importance. NO_2 can have major environmental effects such as contributing to the creation of acid rain, the formation of ground-level ozone, and catalyzing small particles that trigger a range of health problems. For example, exposure to a high concentration of NO_2 can worsen respiratory diseases[1]. In addition to monitoring applications, ultrasensitive chemical sensors can be used for medical diagnoses, such as identifying asthma[2]. Thus, there is a need for more sensitive NO_2 sensors (at the parts per billion (ppb) level) that are both selective and reversible. Common sensor materials are metal oxides[3–5], conducting polymers[6,7], and low-dimensional materials[8–11]. Semiconducting metal oxides have been extensively used for detecting NO_2. However, they usually must operate at high temperatures to achieve an acceptable level of sensitivity[4,5] and satisfactory response and recovery kinetics[12]. This hinders their application due to the increased power consumption.

Two-dimensional (2D) materials[13–20] offer extremely high surface-to-volume ratio, layer-dependent electronic structure, and tunable active sites for redox reactions, making them attractive candidates for gas sensing applications[11,21–25]. Graphene[21] and MoS_2[22,23] have shown excellent sensitivities toward NO_2, but they are not selective and suffer from slow recovery kinetics. Black phosphorus has also been used for gas sensing with an excellent sensitivity for NO_2 down to the ppb level[24]. However, its poor stability and selectivity limit its practical application[24]. 2D tin disulfide (SnS_2) has been shown to be highly sensitive to NO_2 with superior selectivity[25]. The SnS_2 sensor also offers excellent reversibility at 120 °C, but unfortunately does not exhibit acceptable response and recovery times at temperatures below 80 °C[25]. Furthermore,

practical sensors should operate not only at room temperature, but also under conditions of high relative humidity. Humidity greatly deteriorates the sensing properties of metal oxide sensors[26,27] and, to a lesser degree, graphene-based sensors[28]. Therefore, the realization of an ultrasensitive, selective, and reversible NO_2 sensor that can operate in ambient condition (*i.e.* at room temperature and under substantial relative humidity) remains elusive.

Here, we explore the NO_2 sensing behavior of atomically-thin specimens of the transition metal dichalcogenide $Re_{0.5}Nb_{0.5}S_2$. We find that the sensing properties depend sensitively on layer number, with monolayers giving the best overall performance. The monolayer is capable of detecting ultralow concentrations of NO_2 while showing excellent selectivity. Critically, in the presence of humidity, the sensor is highly reversible at room temperature with fast response and recovery times. We explore theoretically the sensor operation for different gas species using density functional theory (DFT), and identify the underlying sensing mechanism.

Bulk crystals of $Re_{0.5}Nb_{0.5}S_2$ are synthesized using chemical vapor transport. The samples are mechanically cleaved to atomic thinness. The cleaved samples remain air stable. Figure 1a shows an annular dark-field scanning transmission electron microscope (ADF-STEM) image of the monolayer $Re_{0.5}Nb_{0.5}S_2$. Owing to the Z (atomic number) contrast of the atomic-resolution image, Re atoms (heavier) show a brighter contrast while Nb atoms (lighter) appear dimmer. In addition, the ADF-STEM image in Fig. 1b reveals an AA′ stacking sequence for bilayer and trilayer regions. Chemical composition of the flake is confirmed from the atomically-resolved ADF-STEM image and complementary energy-dispersive X-ray spectroscopy (EDS) measurements (Fig. 1c and Fig. S1), with near-equal concentration of Re and Nb, as expected for $Re_{0.5}Nb_{0.5}S_2$.

$Re_{0.5}Nb_{0.5}S_2$ offers a broad range of bandgap energies, ranging from ~1.03 eV to ~0.36 eV as the thickness increases from monolayer to bulk[29]. This can result in striking layer-dependent electrical properties. For our sensor platform, different layer number field-effect transistor (FET) devices are fabricated with a two-terminal back-gate configuration (see Fig. 1d and Fig. S2). Prior to sensing measurements, we measure the transport behavior of the FET devices in vacuum. Fig. 1e demonstrates the change in the drain current (I_{ds}) as a function of source-drain bias (V_{ds}) for the monolayer, six-layer (6L), and 30-layer (30L) devices. The linear characteristic of the I_{ds}–V_{ds} curves implies Ohmic contacts. Sweeping the gate voltage, a distinct layer-dependent transport behavior is seen (Fig. 1f). Interestingly, the carrier type of the $Re_{0.5}Nb_{0.5}S_2$ FET devices changes with the layer number, *e.g.* n-type for the monolayer device and p-type for the 6L device. In addition, as the flakes become thicker, the gate control becomes weaker. For instance, the on/off ratio decreases from ~$1.4*10^4$, for the monolayer to ~4 for 6L. The 30L device displays a quasi-metallic behavior with negligible gate control. This can be attributed to the large modification of the $Re_{0.5}Nb_{0.5}S_2$ electronic structure with thickness[29].

For the sensing measurements, we apply a constant source-drain bias (V_{ds}) of 1V to the two-terminal FET devices and monitor the changes in their electrical resistances upon exposure to different concentrations of gas species. The NO_2 molecule, with an unpaired electron, is a strong oxidizer that withdraws electrons from the conduction band of the sensing material, in contrast to electron donor gases (e.g. NH_3, CH_2O) which donate electrons to the sensing material. Consistent with the electrical transport measurements, we observe that the electrical resistance of the monolayer (1L) sensor increases, while that of the 6L sensor decreases, upon the exposure to NO_2. Since the monolayer $Re_{0.5}Nb_{0.5}S_2$ is an n-type semiconductor, the electron transfer from the $Re_{0.5}Nb_{0.5}S_2$ to NO_2 decreases the carrier concentration and hence increases its electrical

resistivity. The 6L device, on the other hand, is a p-type semiconductor and its electrical resistivity decreases upon exposure to NO_2. Figure 2a-b show the responses of the monolayer, 6L, and 30L devices to different NO_2 concentrations ranging from 50 ppb to 15 ppm in dry air. We observe a thickness-dependent response for the $Re_{0.5}Nb_{0.5}S_2$ sensors. While monolayer and 6L devices show excellent responses to NO_2 even at ultra-low concentrations, the 30L sensor is not very sensitive to NO_2. This highlights the importance of surface-to-volume ratio of low-dimensional materials for gas sensing applications. In addition to the surface-to-volume ratio, the drastic change in the electronic structure of $Re_{0.5}Nb_{0.5}S_2$ with the layer number can be another cause of this behavior[29]. We note that metallic single-walled carbon nanotubes (SWNTs) typically show small resistance changes upon exposure to NO_2, while semiconducting SWNTs are capable of detecting small concentrations of NO_2[30]. For the monolayer and 6L $Re_{0.5}Nb_{0.5}S_2$, the response of the sensors almost linearly increases with the NO_2 concentration, as more electrons transfer from $Re_{0.5}Nb_{0.5}S_2$ to NO_2 when the NO_2 concentration is increased.

In order to identify the origin of the carrier type dependence on the $Re_{0.5}Nb_{0.5}S_2$ thickness, we compute the alignments of the energy levels with respect to the vacuum level up to 4 layers. Among several possible low-energy stackings of highly ordered model $Re_{0.5}Nb_{0.5}S_2$, we focus on the three lowest-energy AA´-type stackings (see Fig. S4). The alignment of the valence band and the conduction band edges with respect to the vacuum level for all three stackings is presented in Fig. 2c (see the energy level alignments with the adsorbed NO_2 molecule in Fig. S5). Additionally, we can assume that defect states exist inside the gap in the experimental set up. They can act both as donors and acceptors depending on the chemical potential[31], which is determined by the work function of the metal contacts. In a simplified model, we can assume that all the defect states below the Fermi level of the metal contacts are occupied, and all the defect

states above that level are unoccupied. Since our metal contacts have a work function of ~5 eV, these levels would promote n-type (p-type) behavior in the thinner (thicker) cases, because the change in the conduction band edge is smaller than that in the valence band edge as the thickness increases. This effect of the carrier type change with increasing thickness has been also observed in other 2D materials, such as WSe_2[18,19].

One of the most important characteristics of a chemical sensor is its selectivity to specific molecular species. Fig. 3a shows the responses of the monolayer and 6L sensors to NO_2, NH_3, CH_2O, and CO_2 gases in dry air. Both the 1L and 6L sensors are strongly selective to NO_2 with only minimal responses to the other gases. For instance, responses of the monolayer sensor to NH_3 (1ppm) and CH_2O (2ppm) are found to be ~1.25% and ~2.86%, respectively, while it shows a response of ~34.04% for NO_2 (1 ppm). We also tested the sensitivity of the sensors to 5000ppm CO_2 and found a negligible response to CO_2 (~0.57%).

To understand the selectivity of the $Re_{0.5}Nb_{0.5}S_2$ sensors toward NO_2, we computationally investigate the adsorption of various molecules on the monolayer crystal. We start with 16 random initial configurations for each of the NH_3, CO_2, CH_2O, and NO_2 molecules on $Re_{0.5}Nb_{0.5}S_2$ and allow them to relax to minimize the forces. We find that each molecule is physisorbed, as shown in Fig. 3b-e. The resulting adsorption energies are 0.22, 0.16, 0.19, 0.29 eV for the NH_3, CO_2, CH_2O, and NO_2 molecules, respectively (see details in Supplementary Information and table S1). Since the adsorption energies of the molecules are within the same order of magnitude, the difference in the sensors' response to NO_2 compared to the other molecules is not due to potential differences in coverage. To illuminate the origin of this behavior, we analyze the electronic structure of $Re_{0.5}Nb_{0.5}S_2$ with the adsorbed molecules. In Fig. 3f-i, we present the densities of states for the $Re_{0.5}Nb_{0.5}S_2$ + adsorbed molecule systems. We

observe that NH_3, CO_2 and CH_2O molecules contribute states that are deep in the valence and conduction bands of $Re_{0.5}Nb_{0.5}S_2$, whereas the NO_2 molecule contributes an unoccupied state 0.5 eV above the valence band edge. If $Re_{0.5}Nb_{0.5}S_2$ were an ambipolar semiconductor experimentally, we would expect this state to act as an acceptor state and lead to p-type behavior. However, because of the observed n-type behavior of the monolayer device, we can assume that there are defect states in the gap that are filled up to a level closer to the conduction band edge. In this case, the NO_2 defect state in the gap would accept electrons from these states, reducing the n-type conduction, as experimentally observed. On the other hand, because the other molecules do not generate any gap states, they do not significantly modify the conduction of the system. The unoccupied NO_2 defect state remains close to the valence band edge for the thicker films that we computed (up to 4 layers). Therefore, we expect it to weaken conduction by electrons and strengthen conduction by holes for all thicknesses, as observed. The charge transfer from $Re_{0.5}Nb_{0.5}S_2$ to the molecule is also apparent in the projected densities of state (PDOS) plot in Fig. 3i, as the unoccupied in-gap state has non-zero projection onto the $Re_{0.5}Nb_{0.5}S_2$ states. This can also be observed in the real-space charge transfer plot (Fig. 3j-k).

All the sensing measurements so far described are performed in dry air. Since real-life sensors need to operate under typical atmospheric conditions, we test the monolayer sensor in the presence of humidity. Figure 4a exhibits the dynamic response of the monolayer $Re_{0.5}Nb_{0.5}S_2$ sensor to NO_2 with concentrations ranging from 50 ppb to 15 ppm. Humidity not only does not deteriorate sensing properties of the monolayer device, but also is extremely beneficial for improving its recovery and response to NO_2 at room temperature.

For example, the recovery of the monolayer sensor after exposure to NO_2 (0.5 ppm) is incomplete after being exposed to dry air for 360 s (Fig. S6). However, a complete recovery is

achieved when the sensor is exposed to air with 40% relative humidity (RH) in the same timeframe (Fig. 4a). The response and recovery times, defined as the time required to reach 90% of the resistance change upon exposure to and removal of NO_2 (15 ppm), are approximately ~245 s and ~504 s, respectively, under 40% RH at room temperature. For comparison, an NO_2 sensor based on semiconducting SWNTs was demonstrated to detect 200 ppm of NO_2 with a recovery time of 12 hours at room temperature and 1 hour at 200°C[30]. A metal oxide sensor based on WO_3 detected 500 ppb of NO_2 with recovery times of 270 s and 1350 s at 300 and 150°C, respectively[12]. An NO_2 sensor based on monolayer MoS_2 was recovered to its initial state by leaving it in air for 12 hours at room temperature[23].

In addition to improving the recovery of the $Re_{0.5}Nb_{0.5}S_2$ sensor at room temperature, humidity also largely enhances its response to NO_2. For example, the monolayer $Re_{0.5}Nb_{0.5}S_2$ sensor shows a response of ~195.53% for NO_2 (1 ppm) in the presence of humidity (40% RH), compared to a response of ~34.04% in dry air. Testing the monolayer sensor under different humidity conditions, we see a decrease in the resistance of the device as the relative humidity increases from 0 to 80% (Fig. 4b). This is in contrast to the MoS_2 sensor where an increase in the resistance with humidity was observed[22]. Despite the fact that both the monolayer $Re_{0.5}Nb_{0.5}S_2$ and MoS_2 are n-type semiconductors, they interact with humidity very differently, analogous to the behavior of semiconducting metal oxide sensors. For instance, while a decrease in the resistance with humidity has been observed in n-type gas sensors such as SnO_2 [32] and ZnO [33], WO3, also n-type, has shown an opposite behavior[34].

In order to determine whether the monolayer sensor retains its selectivity to NO_2 in the presence of humidity, we test its response to other gas molecules in air with 40% RH. Fig. 4c displays the responses of the monolayer device to NO_2, NH_3, and CH_2O gases. Even in the

presence of humidity (40% RH), the monolayer sensor is still highly selective to NO_2 with insignificant responses to the other gases. The responses of the monolayer sensor to NH_3 (8ppm) and CH_2O (20ppm) are ~8.77% and ~23.56%, respectively, compared to a response of ~401.86% for NO_2 (5 ppm).

To understand the origins of the improved response and recovery of the monolayer $Re_{0.5}Nb_{0.5}S_2$ sensor in the presence of humidity, we turn to additional theoretical investigations. First, we compute the optimal position of the H_2O molecule to adsorb onto $Re_{0.5}Nb_{0.5}S_2$ (Fig. 4d-e). We then repeat the procedure to find the optimal configurations of higher H_2O coverages (2, 3 and 4 molecules per 4×4 supercell). The adsorption energy per molecule for each coverage is given in Table 1. These calculations suggest that the energetic drive for the water molecules to adsorb onto $Re_{0.5}Nb_{0.5}S_2$ does not diminish even at very high coverage values. For each H_2O coverage, we conduct a further search to find the lowest-energy configuration of the NO_2 adsorption (Fig. 4f-g). To elucidate the energetic drive for NO_2 on the H_2O-covered surface, we compute the adsorption energies as

$$E_{ad} = E_{substrate} + E_{molecule} - E_{substrate+molecule}, \qquad (1)$$

where the substrate is defined as the combination of $Re_{0.5}Nb_{0.5}S_2$ and the already adsorbed H_2O molecules (Table 1). We find that the NO_2 molecules lower their energy by adsorbing near the H_2O molecules (by 0.05 eV for the lowest coverage), indicating a nonzero attraction between the adsorbed molecules. This attraction is due to the intrinsic and induced dipole moments of the molecules and the intermolecular charge transfer. The increase in the NO_2 adsorption energies with H_2O coverage suggests that more NO_2 molecules adsorb onto $Re_{0.5}Nb_{0.5}S_2$ when there are more water molecules available.

The depletion of the $Re_{0.5}Nb_{0.5}S_2$'s charge also increases with H_2O coverage, as listed in Table 1 ($\Delta\rho$ is defined as the total charge transfer from the alloy to the adsorbed molecules). When a water molecule adsorbs onto $Re_{0.5}Nb_{0.5}S_2$, a small amount of charge transfer to the alloy occurs ($\Delta\rho = +0.01e$), as visualized in Fig. 4d-e. However, when the NO_2 molecule adsorbs at a nearby location on $Re_{0.5}Nb_{0.5}S_2$, the charge transfer between the alloy and the molecules is significantly modified (Fig. 4f-g), and $Re_{0.5}Nb_{0.5}S_2$ ends up losing more electrons ($\Delta\rho = -0.12e$) than it does due to the NO_2 molecule alone ($\Delta\rho = -0.10e$). The fact that the charge depletion of the alloy increases with higher H_2O coverage can be visually observed by comparing the PDOS plots in Fig. 3i and Fig. 4h-i, as the projection of the unoccupied in-gap state onto the $Re_{0.5}Nb_{0.5}S_2$ states increases. The fact that both adsorption energy and charge transfer increase with humidity explains the improved response of the monolayer sensor to NO_2 in the presence of humidity.

Regarding the improved recovery rate, we propose a potential mechanism for the desorption of the NO_2 molecules in the presence of humidity driven by the intermolecular dipole-dipole interaction. First, we observe that both NO_2 and H_2O are polar molecules due to their geometry, as opposed to the other molecules prominent in air, *i.e.* N_2 and O_2. By computing electronic structure of the two molecules in isolation, we find $p_{\mathrm{H_2O}} = 1.81$ Debye and $p_{\mathrm{NO_2}} = 0.23$ Debye. If dipole-dipole interaction were the dominant cause of attraction between molecules, this qualitative difference between H_2O and the other atmospheric gases would suggest that the H_2O molecules attract the adsorbed NO_2 molecules while passing close to the alloy's surface, and "sweep" them away, whereas N_2 and O_2 do not. To test this hypothesis, we compute the interaction energies between the molecular pairs. For NO_2 and H_2O, this interaction energy (ΔE), defined as

$$\Delta E = E_{\mathrm{NO_2+H_2O}} - E_{\mathrm{NO_2}} - E_{\mathrm{H_2O}}, \quad (2)$$

is -0.046 eV and -0.029 eV when their dipole moments are aligned and anti-aligned, respectively. In the absence of induced dipole moments, the difference between the two values would be equal to twice the dipole-dipole interaction energy ($E_{d-d} = -0.008$ eV). From basic electrostatics, this energy can be estimated using the dipole moments of the molecules and the intermolecular distance ($\Delta z = 3.45$ Å), which yields $E_{d-d,\mathrm{estimated}} = -0.012$ eV. The difference between the two E_{d-d} values suggests that the induced dipole moments are non-negligible and may cause similar levels of attraction between NO_2 and non-polar molecules. In Table 2, we list the ΔE and $p_{induced}$ values for the interaction between NO_2 and all three atmospheric gases. We find that both the attraction and the induced dipole moment of H_2O is significantly greater than N_2 and O_2. Repeating these calculations on $Re_{0.5}Nb_{0.5}S_2$, where the NO_2 molecule is adsorbed optimally with its dipole moment points away from the alloy, yields the same comparison between the three atmospheric gases. Therefore, we suggest that the significant improvement of the recovery rate may be due to the attraction between the polar H_2O molecules and the adsorbed NO_2 molecules, which is significantly greater than those for N_2 and O_2.

In summary, we have demonstrated an NO_2 sensor based on a monolayer semiconducting alloy that has the advantage of room-temperature finite-humidity operation and ppb sensitivity. The monolayer sensor is highly selective to NO_2 with only minimal responses to other gases. In the presence of humidity, the monolayer sensor is highly reversible at room temperature with fast recovery time. Humidity also largely enhances the response of the sensor to NO_2 due to the increased charge transfer by the co-adsorption of the NO_2 and H_2O molecules onto the monolayer crystal. Furthermore, our atomically-thin $Re_{0.5}Nb_{0.5}S_2$ sensor is flexible and optically

transparent, making it attractive for a wide range of low-power sensor applications, such as in wearable electronics.

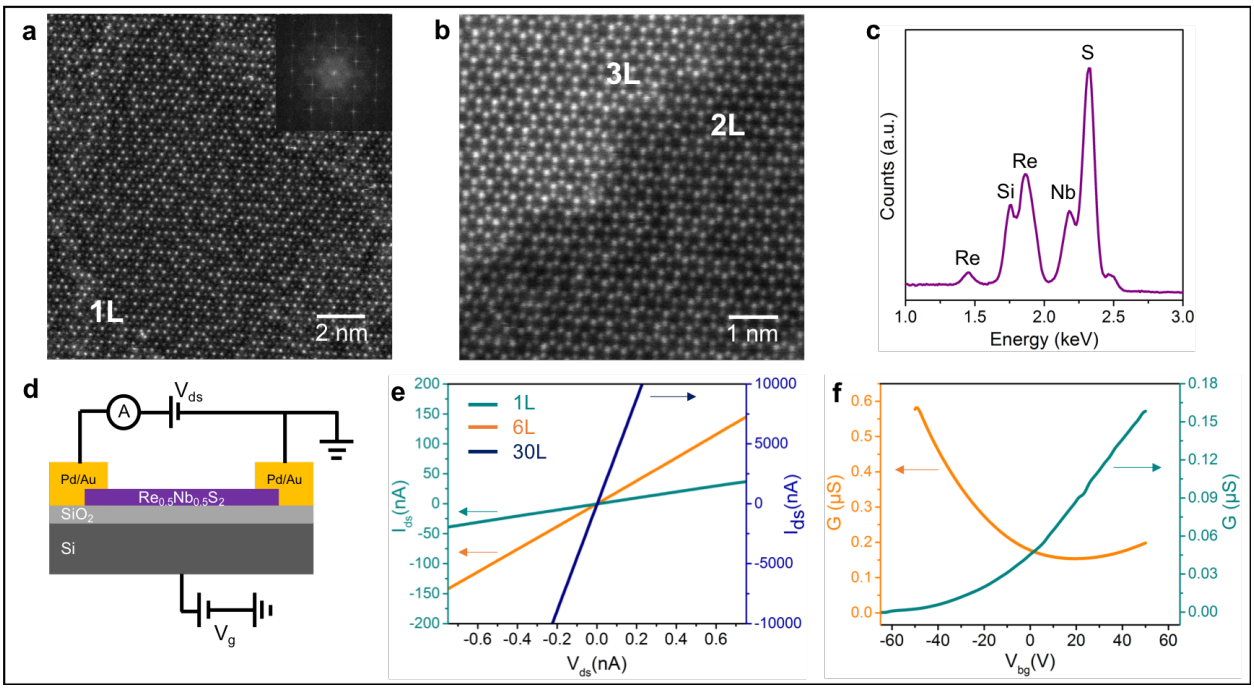

Fig. 1 | Atomic structure, chemistry, and electrical characteristics of $Re_{0.5}Nb_{0.5}S_2$. **a**, An ADF-STEM image of the monolayer $Re_{0.5}Nb_{0.5}S_2$ with the corresponding FFT (inset). **b**, An atomic-resolution ADF-STEM image of the bilayer and trilayer regions of $Re_{0.5}Nb_{0.5}S_2$ revealing its stacking order. **c**, EDS spectrum from a few-layer $Re_{0.5}Nb_{0.5}S_2$ crystal (see Fig. S1) showing peaks of Re, Nb, S, and Si (from the silicon nitride TEM grid). **d**, Schematic of the NO_2 sensors based on an FET device with a two-terminal back-gate configuration. **e**, Drain current (I_{ds}) as a function of source-drain bias (V_{ds}) for the monolayer, 6L, and 30L devices. **f**, Conductance (G) of the monolayer, and 6L devices as a function of the gate voltage (V_{bg}).

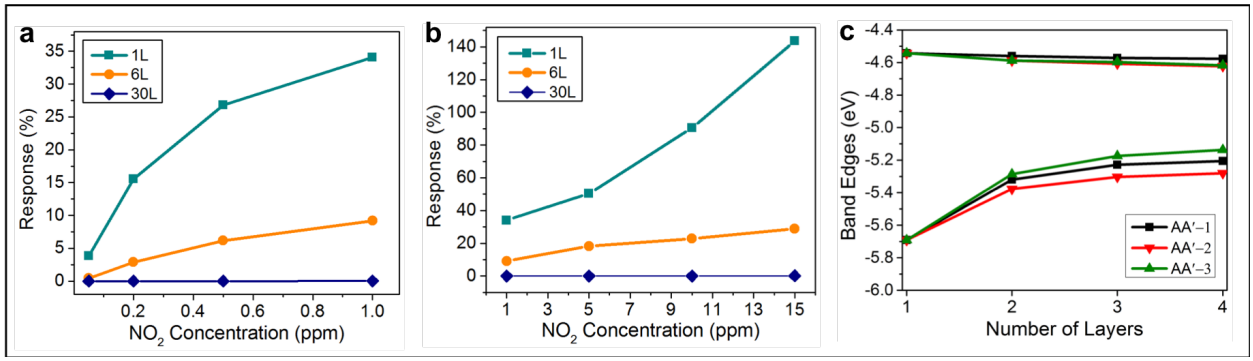

Fig. 2 | Layer-dependent behavior of $Re_{0.5}Nb_{0.5}S_2$ NO_2 sensors. The responses of the monolayer, 6L, and 30L devices to different NO_2 concentrations raging from **a**, 50 ppb to 1 ppm and **b**, 1 to

15 ppm in dry air. Response is defined as $S = (R_g - R_{air})/R_{air}$, with R_g and R_{air} being the resistance of the device in target gas and air, respectively. **c**, The alignment of the valence band and the conduction band edges with respect to the vacuum level for three AA´-type stackings (see Fig. S4).

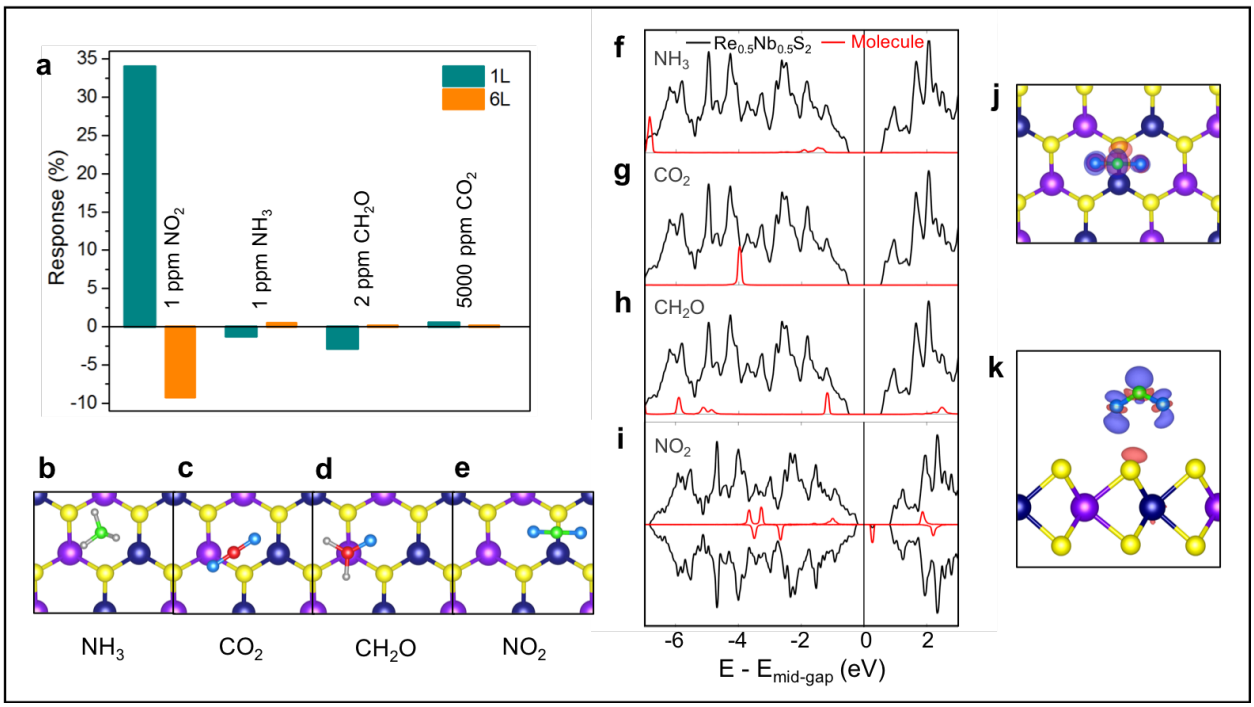

Fig. 3 | Selectivity of the $Re_{0.5}Nb_{0.5}S_2$ sensors toward NO_2. **a**, The responses of the 1L and 6L sensors to NO_2, NH_3, CH_2O, and CO_2 gases in dry air. **b-e**, NH_3, CO_2, CH_2O, and NO_2 molecules being physisorbed on the monolayer crystal. **f-i**, The densities of states for the $Re_{0.5}Nb_{0.5}S_2$ and the adsorbed NH_3, CO_2, CH_2O, and NO_2 molecule systems. Projections onto the atomic orbitals are used to distinguish between the molecular states and the states in the substrate. The NO_2 molecule causes spin polarization in the system, and hence the two spins are plotted separately. **j-k**, The real-space charge transfer plot showing the charge transfer from $Re_{0.5}Nb_{0.5}S_2$ to the NO_2 molecule. Re: navy, Nb: violet, S: yellow, N: green, H: grey, O: blue, C: red.

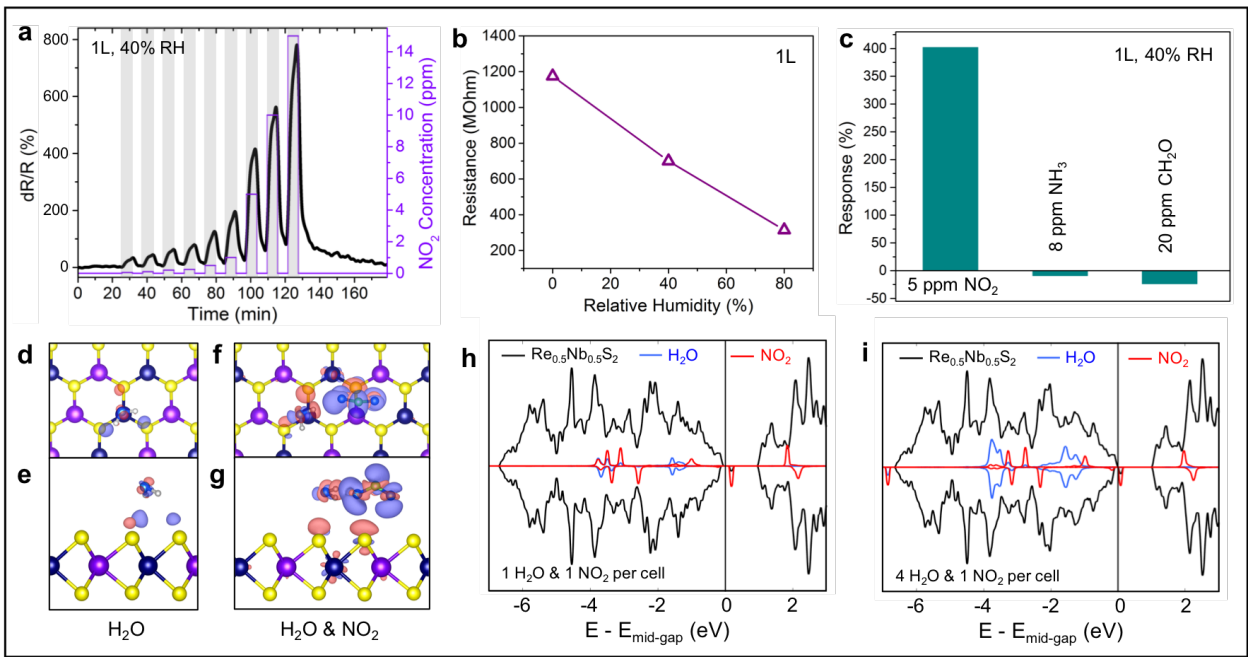

Fig. 4 | Humidity impacts on the monolayer sensor. a, Dynamic response of the monolayer $Re_{0.5}Nb_{0.5}S_2$ sensor to NO_2 with concentrations ranging from 50 ppb to 15 ppm under 40% RH condition at room temperature. **b**, Change in the resistance of the monolayer sensor as a function of the relative humidity. **c**, Responses of the monolayer device to NO_2, NH_3, and CH_2O gases in presence of humidity (40% RH). **d-e**, The optimal position of the H_2O molecule to adsorb onto the monolayer $Re_{0.5}Nb_{0.5}S_2$. **f-g**, The lowest-energy configuration of the NO_2 adsorption on the alloy for each H_2O coverage. **h-i**, The PDOS plots for the $Re_{0.5}Nb_{0.5}S_2$ and the adsorbed NO_2 and H_2O molecules, showing an increase in the charge depletion of $Re_{0.5}Nb_{0.5}S_2$ with higher H_2O coverage. Re: navy, Nb: violet, S: yellow, N: green, H: grey, O: blue.

H_2O coverage per 4×4 cell	**0**	**1**	**2**	**3**	**4**
E_{ad}**(H_2O) (eV)**		0.16	0.16	0.15	0.14
E_{ad}**(NO_2) (eV)**	0.29	0.34	0.41	0.42	0.51
$\Delta\rho$	-0.10e	-0.12e	-0.14e	-0.14e	-0.16e

Table 1 | Computed adsorption energies of H_2O and NO_2 molecules on the $Re_{0.5}Nb_{0.5}S_2$ alloy, under various H_2O coverages, and the charge transfer from the alloy to the adsorbed molecules. The first (top) row lists the number of adsorbed H_2O molecules in the 4×4 cell. The second row lists the adsorption energy of the nth H_2O molecule in the cell. The third row lists the adsorption energy of the NO_2 molecule with n H_2O molecules already adsorbed onto $Re_{0.5}Nb_{0.5}S_2$. The entries in the fourth row correspond to the configurations in the third row, and list the charge transfer from the alloy to the adsorbed molecules, after the adsorption of all the molecules (NO2 $+ n \times$ H_2O).

Molecule interacting with NO_2	H_2O	N_2	O_2
ΔE in vacuum (eV)	-0.046	-0.014	-0.021
$p_{induced}$ in vacuum (D)	0.34	0.04	0.10
ΔE on alloy (eV)	-0.012	-0.004	-0.007
$p_{induced}$ on alloy (D)	0.23	0.03	0.08

Table 2 | Computed interaction energies of H_2O, N_2 and O_2 with NO_2 and the induced dipole moment in each case. The second row of the table lists the interaction energies, defined as $\Delta E = E_{\mathrm{NO_2+H_2O}} - E_{\mathrm{NO_2}} - E_{\mathrm{H_2O}}$ for H_2O, and similarly for the other molecules. The third row of the table lists the induced dipole moment for each of these configurations. The fourth row is analogous to the second, but with the initial NO_2 molecule adsorbed onto $Re_{0.5}Nb_{0.5}S_2$, as shown in Fig. 3j-k. To compute ΔE, the additional molecule (H_2O, N_2 or O_2) is placed on top of the already-adsorbed NO_2 molecule and the atoms are allowed to relax. Here, $\Delta E = E_{\mathrm{alloy+NO_2+H_2O}} - E_{\mathrm{alloy+NO_2}} - E_{\mathrm{H_2O}}$ for H_2O, and similar for the other molecules. The fifth row lists the induced dipole moment for each of these configurations.

Acknowledgements

This work was primarily supported by the U.S. Department of Energy, Office of Science, Office of Basic Energy Sciences, Materials Sciences and Engineering Division under Contract No. DE-AC02-05-CH11231, within the sp2-bonded Materials Program (KC2207), which provided for materials synthesis, chemical sensitivity tests, and atomic structure calculations. Additional support was provided by the National Science Foundation under Grant No. DMR-1807233 which provided for STEM measurements, and under Grant No. DMR-1926004 which provided for calculations of precise electronic structures. Computational resources were provided by the DOE at Lawrence Berkeley National Laboratory's NERSC facility and the NSF through XSEDE resources at NICS. We thank Sehoon Oh for fruitful scientific discussions.

References

1. Belanger, K., Gent, J. F., Triche, E. W., Bracken, M. B. & Leaderer, B. P. Association of Indoor Nitrogen Dioxide Exposure with Respiratory Symptoms in Children with Asthma. *Am. J. Respir. Crit. Care Med.* **173**, 297–303 (2006).
2. Yoon, J.-W. & Lee, J.-H. Toward breath analysis on a chip for disease diagnosis using semiconductor-based chemiresistors: recent progress and future perspectives. *Lab Chip* **17**, 3537–3557 (2017).
3. Meixner, H. & Lampe, U. Metal oxide sensors. *Sensors Actuators B Chem.* **33**, 198–202 (1996).
4. Afzal, A., Cioffi, N., Sabbatini, L. & Torsi, L. NOx sensors based on semiconducting metal oxide nanostructures: Progress and perspectives. *Sensors Actuators B Chem.* **171**–

172, 25–42 (2012).
5. Pinna, N., Neri, G., Antonietti, M. & Niederberger, M. Nonaqueous Synthesis of Nanocrystalline Semiconducting Metal Oxides for Gas Sensing. *Angew. Chemie Int. Ed.* **43**, 4345–4349 (2004).
6. Miasik, J. J., Hooper, A. & Tofield, B. C. Conducting polymer gas sensors. *J. Chem. Soc. Faraday Trans. 1 Phys. Chem. Condens. Phases* **82**, 1117 (1986).
7. Janata, J. & Josowicz, M. Conducting polymers in electronic chemical sensors. *Nat. Mater.* **2**, 19–24 (2003).
8. Collins, P. G. Extreme Oxygen Sensitivity of Electronic Properties of Carbon Nanotubes. *Science (80-.).* **287**, 1801–1804 (2000).
9. Modi, A., Koratkar, N., Lass, E., Wei, B. & Ajayan, P. M. Miniaturized gas ionization sensors using carbon nanotubes. *Nature* **424**, 171–174 (2003).
10. Banan Sadeghian, R. & Saif Islam, M. Ultralow-voltage field-ionization discharge on whiskered silicon nanowires for gas-sensing applications. *Nat. Mater.* **10**, 135–140 (2011).
11. Meng, Z., Stolz, R. M., Mendecki, L. & Mirica, K. A. Electrically-Transduced Chemical Sensors Based on Two-Dimensional Nanomaterials. *Chem. Rev.* **119**, 478–598 (2019).
12. Heidari, E. K., Zamani, C., Marzbanrad, E., Raissi, B. & Nazarpour, S. WO3-based NO2 sensors fabricated through low frequency AC electrophoretic deposition. *Sensors Actuators B Chem.* **146**, 165–170 (2010).
13. Azizi, A. *et al.* Freestanding van der Waals Heterostructures of Graphene and Transition Metal Dichalcogenides. *ACS Nano* **9**, 4882–4890 (2015).
14. Azizi, A. *et al.* Dislocation motion and grain boundary migration in two-dimensional tungsten disulphide. *Nat. Commun.* **5**, 4867 (2014).
15. Wang, Q. H., Kalantar-Zadeh, K., Kis, A., Coleman, J. N. & Strano, M. S. Electronics and optoelectronics of two-dimensional transition metal dichalcogenides. *Nat. Nanotechnol.* **7**, 699–712 (2012).
16. Azizi, A. *et al.* Spontaneous Formation of Atomically Thin Stripes in Transition Metal Dichalcogenide Monolayers. *Nano Lett.* **16**, 6982–6987 (2016).
17. Azizi, A. *et al.* Layer-Dependent Electronic Structure of Atomically Resolved Two-Dimensional Gallium Selenide Telluride. *Nano Lett.* **19**, 1782–1787 (2019).
18. Zhou, C. *et al.* Carrier Type Control of WSe2 Field-Effect Transistors by Thickness Modulation and MoO3 Layer Doping. *Adv. Funct. Mater.* **26**, 4223–4230 (2016).
19. Pudasaini, P. R. *et al.* High-performance multilayer WSe2 field-effect transistors with carrier type control. *Nano Res.* **11**, 722–730 (2018).
20. Azizi, A. *et al.* Defect Coupling and Sub-Angstrom Structural Distortions in W 1– x Mo x S 2 Monolayers. *Nano Lett.* **17**, 2802–2808 (2017).
21. Schedin, F. *et al.* Detection of individual gas molecules adsorbed on graphene. *Nat. Mater.* **6**, 652–655 (2007).
22. Late, D. J. *et al.* Sensing Behavior of Atomically Thin-Layered MoS 2 Transistors. *ACS Nano* **7**, 4879–4891 (2013).
23. Liu, B. *et al.* High-Performance Chemical Sensing Using Schottky-Contacted Chemical Vapor Deposition Grown Monolayer MoS 2 Transistors. *ACS Nano* **8**, 5304–5314 (2014).
24. Abbas, A. N. *et al.* Black Phosphorus Gas Sensors. *ACS Nano* **9**, 5618–5624 (2015).
25. Ou, J. Z. *et al.* Physisorption-Based Charge Transfer in Two-Dimensional SnS2 for Selective and Reversible NO2 Gas Sensing. *ACS Nano* **9**, 10313–10323 (2015).

26. Neri, G., Bonavita, A., Galvagno, S., Siciliano, P. & Capone, S. CO and NO2 sensing properties of doped-Fe2O3 thin films prepared by LPD. *Sensors Actuators B Chem.* **82**, 40–47 (2002).
27. Ling, Z. & Leach, C. The effect of relative humidity on the NO2 sensitivity of a SnO2/WO3 heterojunction gas sensor. *Sensors Actuators B Chem.* **102**, 102–106 (2004).
28. Kim, Y. H. *et al.* Self-Activated Transparent All-Graphene Gas Sensor with Endurance to Humidity and Mechanical Bending. *ACS Nano* **9**, 10453–10460 (2015).
29. Azizi, A; Dogan, M; Cain, JD; Eskandari, R; Yu, X; Glazer, EC; Cohen, ML; Zettl, A. Frustration and atomic ordering in a monolayer semiconductor alloy. *Phys. Rev. Lett.* (2020).
30. Kong, J. Nanotube Molecular Wires as Chemical Sensors. *Science (80-.).* **287**, 622–625 (2000).
31. Dolui, K., Rungger, I. & Sanvito, S. Origin of the n-type and p-type conductivity of MoS2 monolayers on a SiOs substrate. *Phys. Rev. B* **87**, 165402 (2013).
32. Degler, D., Wicker, S., Weimar, U. & Barsan, N. Identifying the Active Oxygen Species in SnO 2 Based Gas Sensing Materials: An Operando IR Spectrsocopy Study. *J. Phys. Chem. C* **119**, 11792–11799 (2015).
33. Zhang, Y. *et al.* Zinc oxide nanorod and nanowire for humidity sensor. *Appl. Surf. Sci.* **242**, 212–217 (2005).
34. Staerz, A. *et al.* The oxidizing effect of humidity on WO3 based sensors. *Sensors Actuators B Chem.* **237**, 54–58 (2016).